American Mineralogist, Volume 94, pages 950–956, 2009

Phase behavior of protoenstatite at high pressure studied by atomistic simulations

Sandro Jahn[1,*] and Roman Martoňák[2]

[1]Deutsches GeoForschungsZentrum (GFZ), Section 3.3, Telegrafenberg, 14473 Potsdam, Germany
[2]Department of Experimental Physics, Faculty of Mathematics, Physics and Informatics, Comenius University, Mlynská dolina F2, 84248 Bratislava, Slovakia

Abstract

Structural phase transformations of $MgSiO_3$ protoenstatite at high pressures are studied by atomic scale simulation techniques. Molecular-dynamics simulations and electronic-structure calculations reveal two metastable polymorphs with space groups $P2_1cn$ and $Pbcn$, respectively. They are related to protoenstatite by displacive transition mechanisms via subsequent change of the silicate chain rotations from O- to S-type. Metadynamics simulations in combination with molecular dynamics reveal possible mechanisms for the martensitic transition from protoenstatite to high-pressure clinoenstatite. Two different shear mechanisms in the (100) plane are activated during the transition. The first consists of four partial displacements in (100)[001] and (100)[010], whereas in a second step only a single shear in (100)[001] is observed.

Keywords: Molecular dynamics, metadynamics, phase transition, enstatite, $MgSiO_3$, protopyroxene, clinopyroxene

Introduction

Pyroxenes are important crustal and upper mantle minerals (Ringwood 1975; Anderson 1989). Their common structural features are tetrahedral chains usually of SiO_4 units that are separated by parallel chains of octahedral edge-sharing $M1O_6$ units containing cations on the M1 site. Differences between pyroxene structures such as the stacking sequence of the chains, the rotation angles within the chains or the oxygen coordination of cations on the second site, M2, (Downs 2003) control the physical properties of the respective crystals, e.g., their density or elastic properties, and thus influence geophysical and rheological properties of crustal and upper mantle rocks.

The thermodynamic stability of different pyroxene structures depends on P, T, and chemical composition. Enstatites with $MgSiO_3$ composition are known to exist in at least five different structures (Fig. 1). At low T and low P, monoclinic low-clinoenstatite with space group $P2_1/c$ is the stable phase. A displacive phase transition at high P results in high-P clinoenstatite with space group $C2/c$ (Angel et al. 1992). Orthoenstatite (*Pbca*) occurs at high T and pressures up to about 7 GPa, whereas protoenstatite (*Pbcn*) and high-T clinoenstatite ($C2/c$) have small stability fields at high T and low P (Presnall 1995).

Crystallographic considerations suggest several additional pyroxene phases (Thompson and Downs 2003), some of which may exist as metastable enstatite phases. For instance, experimental (Lin 2003; Kung et al. 2004) and atomistic simulation studies (Jahn 2008) suggest at least one high-pressure orthoenstatite phase. Other phases have stability fields at compositions slightly different from enstatite such as high-T orthopyroxene (*Pbca*) of $(Ca_{0.06}Mg_{1.94})Si_2O_6$ (Ohi et al. 2008) or high-P protopyroxene ($P2_1cn$) of $(Mg_{1.54}Li_{0.23}Sc_{0.23})Si_2O_6$ (Yang et al. 1999).

For a systematic understanding of the complex phase behavior in pyroxenes, not only the thermodynamics have to be known, but also the kinetics of the transitions may be of importance. Transmission electron microscopy has been used extensively to study the transitions in pyroxenes, especially from orthopyroxene to clinopyroxene (Coe and Müller 1973; Coe and Kirby 1975; McLaren and Etheridge 1976; Hugh-Jones et al. 1996). It was concluded that the dominant transition mechanism is

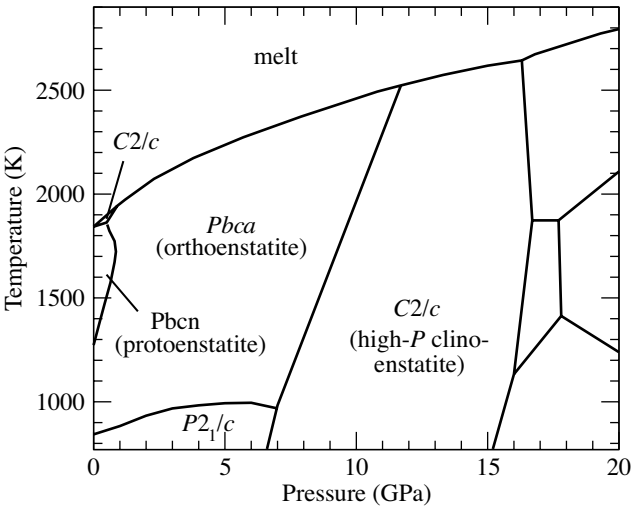

Figure 1. Part of the $MgSiO_3$ phase diagram that contains the stability of five different enstatite phases (after Presnall 1995). Other pyroxene phases discussed here, especially the high-pressure phases of protoenstatite and orthoenstatite are metastable phases.

* E-mail: jahn@gfz-potsdam.de

a slip parallel to the close-packed oxygen layers in the (100) plane along the silicate chains, i.e., in [001] direction. A recent simulation study suggests shear components in [001] and [010] directions although the latter may be difficult to observe (Jahn and Martoňák 2008).

The protoenstatite to ortho-/clinoenstatite transition was studied by neutron scattering (Schrader et al. 1990; Boysen et al. 1991). During cooling, the protoenstatite reverts to ortho- or low-clinoenstatite depending on cooling rate. It is concluded that stacking faults are created with the onset of the transition and that they are a consequence of the transformation (Schrader et al. 1990).

Here we extend our previous simulation studies of the high-pressure behavior of orthoenstatite (Jahn 2008) and the ortho- to high-pressure clinoenstatite transition (Jahn and Martoňák 2008) in a systematic way to protoenstatite. The atomic scale-modeling approach provides direct access to the transformation process, which goes beyond experimental capabilities.

Computational details

Molecular dynamics (MD) simulations are performed using an advanced ionic interaction model (AIM) that accounts for anion polarization and shape deformations (Aguado et al. 2003; Madden et al. 2006). The AIM potential is optimized by reference to electronic structure calculations and has been shown to be accurate and transferable in a wide range of pressures, temperatures, and compositions of the Ca-Mg-Al-Si-O system (Jahn and Madden 2007). It reproduces well the lattice parameters and elastic constants of various $MgSiO_3$ polymorphs (Jahn and Madden 2007; Jahn and Martoňák 2008) and predicts correctly the transition pressure of the low- to high-P clinoenstatite displacive phase transition (Jahn and Madden 2007).

The simulation cell for the MD and metadynamics simulations contains 640 ions, i.e., 128 formula units of $MgSiO_3$. Temperature and pressure are controlled by a Nose-Hoover thermostat coupled to a barostat (Martyna et al. 1994). For the numerical integration of the equation of motion, a time step of $\Delta t = 1$ fs is used.

For the metadynamics simulations, an algorithm described in Martoňák et al. (2006) is applied, which employs the components of the scaled box matrix as collective variables. The external pressure is fixed to $P = 15$ GPa, which is at the high-pressure end of the high-P clinoenstatite stability field. The initial configuration is obtained from an MD run at this pressure and $T = 1000$ K in the *NPT* ensemble. The temperature of 1000 K is chosen to be high enough to speed up the transition kinetics and to be well below the melting point to prevent amorphization of the crystal during deformation. At each metadynamics step a short (1 ps) MD run in the *NVT* ensemble, i.e., at constant volume, is performed to relax the atomic positions and calculate the average stress tensor as required by the metadynamics algorithm. The respective temperature of 1000 K is controlled by the thermostat. As metadynamics parameter, a Gaussian height of 8.32 eV is used, which corresponds to 0.065 eV per MgSiO unit. The Gaussian width is 2.88 $eV^{1/2}$. The scaled coordinates are defined using the Hessian matrix calculated for the initial configuration. In total, 1000 metadynamics steps are performed.

Finally, electronic structure calculations are performed in the framework of density functional theory (DFT) using the planewave code ABINIT (Gonze et al. 2002, 2005). The exchange correlation functional is treated in the local density approximation (LDA) (Perdew and Zunger 1981). Optimized norm-conserving pseudopotentials (Rappe et al. 1990) are generated with the OPIUM code and a planewave energy cutoff of 1000 eV is chosen. The Brillouin zone of the primitive lattice is sampled with suitable Monkhorst-Pack grid (Monkhorst and Pack 1976). All DFT calculations are performed in the athermal limit ($T = 0$ K) using the respective crystal unit cells as simulation cell. For the calculation of the enthalpy curves, cell parameters, and atomic positions of the different structures are optimized at various pressures.

Results

Molecular dynamics

In a first step, the response of protoenstatite to hydrostatic pressure, is studied by MD simulation at constant temperature of 1000 K. The evolution of the volume during compression and decompression and the cell parameters are shown in Figures 2 and 3, respectively. The corresponding cell angles fluctuate around 90° over the whole length of the MD simulation and hence the simulation cell remains orthorhombic. The cell volume (Fig. 2) decreases monotonically with pressure. During compression, a sudden drop in volume by about 3% is observed at 19 GPa. The jump in volume is reversed on the decompression path at about 12 GPa, which is indicative of a displacive phase transition with some hysteresis due to activation energy. The lower volume is entirely due to compression in the direction of the c lattice parameter, i.e., along the direction of the SiO_4 chains. The lattice parameters, a and b, that are perpendicular to the chain direction

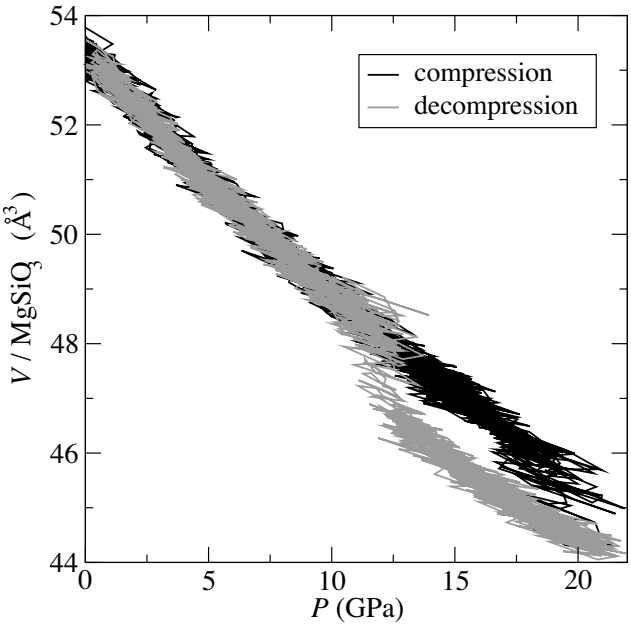

Figure 2. Evolution of the volume per formula unit of protoenstatite during compression and decompression as observed during MD simulations at $T = 1000$ K.

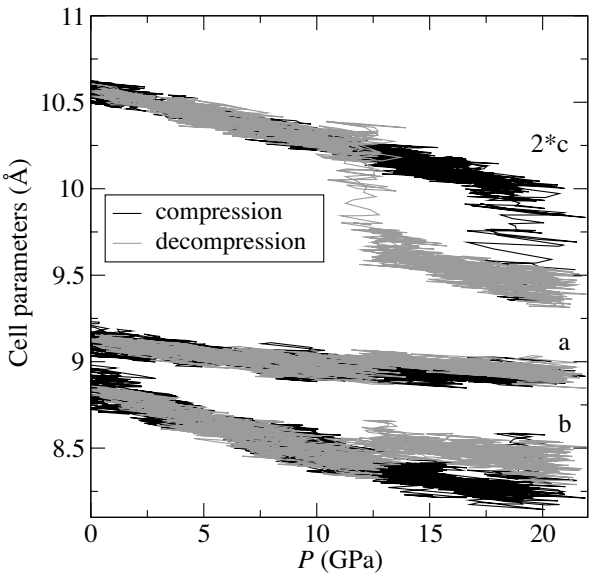

FIGURE 3. Evolution of the cell parameters *a*, *b*, and *c* of protoenstatite during compression and decompression as observed during MD simulations at $T = 1000$ K.

are almost unchanged or even increase slightly (see Fig. 3).

The unit cell of the high-pressure phase is extracted after quenching the simulation cell to low temperature by inspecting the periodicity of the crystal structure. Since the number of periodic units in the supercell, as well as the symmetry are unaltered, the high-pressure phase remains in space group *Pbcn*. The unit cell of this phase is used as a starting configuration in the subsequent DFT calculations. We call this new phase *Pbcn*-II.

DFT calculations

Due to the small energetic differences between pyroxene structures, we rely on the accuracy of electronic structure calculations rather than on classical interaction potentials for the calculation of the thermodynamic stability fields of the various structures. In the athermal limit, i.e., at $T = 0$ K, the most stable phase at a given pressure is the phase with the lowest enthalpy. As candidate structures we consider protoenstatite, *Pbcn*, the high-pressure phase found in the MD simulation, *Pbcn*-II, the "ideal" pyroxene structure and potential high-pressure phase with space group $P2_1cn$. In addition, we use previous data on orthoenstatite *Pbca*, low-clinoenstatite $P2_1/c$, and high-pressure clinoenstatite $C2/c$ (Jahn 2008).

The lattice parameters and cell volumes of the protoenstatite derived phases from the DFT-LDA calculations at ambient pressure are given in Table 1. The high-pressure phases are denser than protoenstatite with a decrease in volume by 2.5 and 5.1% for the $P2_1cn$ and *Pbcn*-II phases, respectively. The DFT calculations confirm that the compression is almost entirely in the *c* direction. Figures 4 and 5 compare the cell volumes and the enthalpies of the different phases. Whereas the $P2_1cn$ phase is comparable in volume to orthoenstatite and low-clinoenstatite, the density of the *Pbcn*-II phase is close to that of high-pressure clinoenstatite over the whole pressure range considered. As expected, all protoenstatite related phases are metastable at $T = 0$ K. The thermodynamically stable phases in the athermal limit, i.e., the lowest enthalpy structures in Figure 5, are low-clinoenstatite with space group $P2_1/c$ below about 3 GPa and $C2/c$ high-pressure clinoenstatite above 3 GPa. The $P2_1cn$ phase is predicted to be comparable in enthalpy to *Pbcn* even close to ambient pressure. It remains the most stable of the protoenstatite related phases up to about 18 GPa, where the *Pbcn*-II phase becomes more stable.

Metadynamics

The combined approach of molecular dynamics and metadynamics provides insight into possible transition paths for the phase transition between protoenstatite and high-pressure clinoenstatite. The evolution of simulation cell parameters and enthalpy after each metadynamics step are shown in Figures 6a, 6c, and 6e. The enthalpy curve (Fig. 6e) has two distinct minima, one around 450 and the other around 700 metadynamics steps. The first is accompanied by sudden changes in the simulation cell parameters, especially in γ (Fig. 6a) and *a* (Fig. 6c). The large fluctuations in all three diagrams are due to non-hydrostatic strains exerted on the cell during metadynamics. A clearer picture of the structural changes is obtained after relaxation of the simulation cell after each step to hydrostatic pressure conditions and after removing kinetic energy from the system by quenching the temperature from 1000 to 300 K in short MD simulations. At ambient temperature the thermal fluctuations are small and hence the energetics are expected to be dominated by the enthalpy term of the free energy.

The thus obtained simulation cell parameters and enthalpies are shown in Figures 6b, 6d, and 6f. The final structure that is obtained in metastep 672 and which remains essentially unchanged until 1000 metasteps has a lower enthalpy than the initial

TABLE 1. Lattice and structural parameters of protoenstatite *Pbcn* and derived high-pressure phases $P2_1cn$ and *Pbcn*-II at $P = 0$ GPa and $T = 0$ K from DFT calculations

Phase	*Pbcn*	*Pbcn*-II	$P2_1cn$		
a (Å)	9.171	9.177	9.039		
b (Å)	8.513	8.816	8.695		
c (Å)	5.254	4.812	5.089		
V (Å)	410.2	389.3	400.0		
O1 x	0.1181	0.1218	0.1210	0.8784	O4 x
O1 y	0.0947	0.0928	0.0864	0.9087	O4 y
O1 z	0.0792	0.1110	0.0589	0.8751	O4 z
O2 x	0.3758	0.3772	0.3769	0.6214	O5 x
O2 y	0.2519	0.2379	0.2460	0.7603	O5 y
O2 z	0.0697	0.0759	0.1056	0.9587	O5 z
O3 x	0.3493	0.3502	0.3578	0.6464	O6 x
O3 y	0.9763	0.0542	0.9609	0.9517	O6 y
O3 z	0.2928	0.4892	0.2760	0.5622	O6 z
Si1 x	0.2913	0.2930	0.2967	0.7019	Si2 x
Si1 y	0.0920	0.0927	0.0887	0.9104	Si2 y
Si1 z	0.0679	0.1732	0.0684	0.8620	Si2 z
Mg1 x	0	0	0.9975		
Mg1 y	0.0944	0.0962	0.0961		
Mg1 z	0.75	0.75	0.7160		
Mg2 x	0	0	0.0060		
Mg2 y	0.2666	0.2767	0.2627		
Mg2 z	0.25	0.25	0.2151		

Notes: The respective Wyckoff positions are (8*d*) for O1, O2, O3, Si1; (4*c*) for Mg1, Mg2 of *Pbcn* and *Pbcn*-II; and (4*a*) for all atoms of $P2_1cn$. For comparison of the different structures, the origin of space group $P2_1cn$ has been shifted by [0 0.25 0] with respect to the standard setting in the *International Tables for X-ray Crystallography* (Henry and Lonsdale 1965).

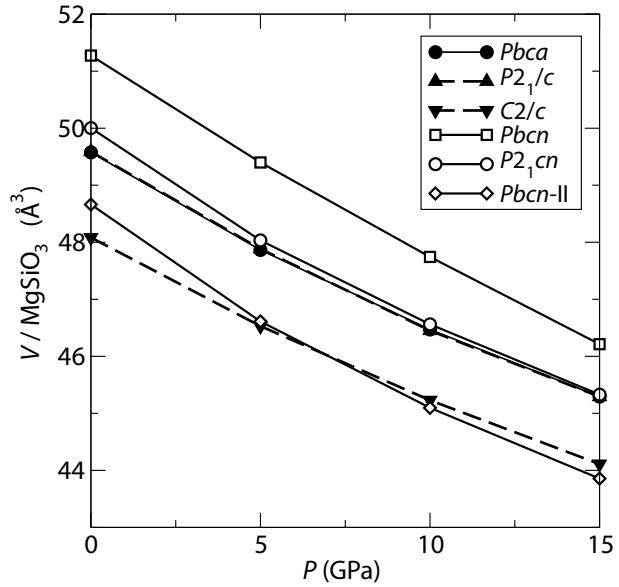

FIGURE 4. Volume per formula unit of different enstatite phases from DFT calculations as a function of pressure. The volumes of orthoenstatite *Pbca* and low-clinoenstatite $P2_1/c$ fall on the same line.

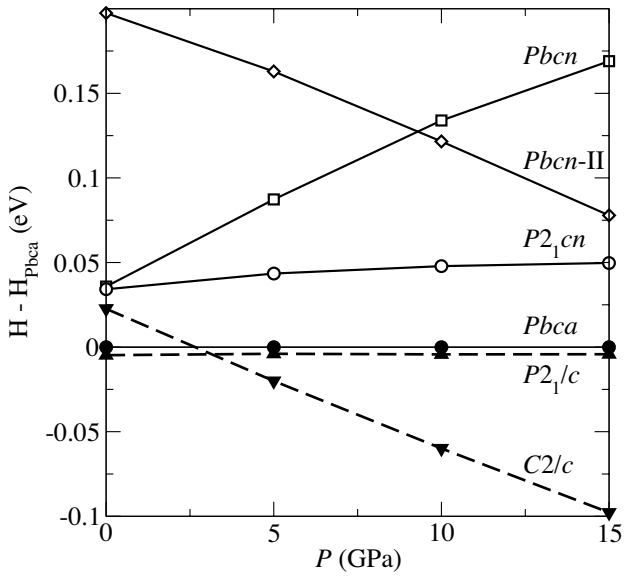

FIGURE 5. Phase stability of different enstatite phases from DFT calculations at $T = 0$ K as a function of pressure. In this representation, enthalpy differences with respect to orthoenstatite *Pbca* are shown.

protoenstatite, which is observed between metasteps 1 and 356. This final structure is identified as high-pressure clinoenstatite, i.e., the expected stable phase at 15 GPa. The small dips in enthalpy in metastep 1, between metasteps 300 and 304 and in metastep 353 correspond to occurrence of the *Pbcn*-II phase as discussed above. This phase also leads to changes in the lattice parameters *a* and *c* (Fig. 6d) but there is no change in the cell angles (Fig. 6b).

The transition from proto- to high-*P* clinoenstatite apparently happens in the two regions of the enthalpy minima of Figure 6e. In the first region between metasteps 357 and 417, four shear deformations take place that can be identified by jumps in the lattice parameters in Figures 6b and 6d. These deformations are shears in the (100) plane, which add up to a total displacement of one crystal unit cell in [010] and about 1/3 unit cells in [001]. The intermediate structures possess high energy as can be seen in Figure 6f.

The second region of deformation consists essentially of a single shear in (100)[001] but in a different (100) plane of the simulation cell. The total displacement vector is about –2/3 [001], i.e., in an opposite sense and with a larger magnitude in [001] compared to the first deformation region but also without shear component in [010]. This shear happens at metastep 672. Jumps in enthalpy not related to deformations of the simulation cell (e.g., at metastep 620) are due to annealing of Mg point defects. The latter are remnants of a diffusive Mg cation reorganization in the shear plane that sets in when Mg-O bonds are broken due to the shear deformations.

CONCLUDING REMARKS

The sequence of (pseudo)stability fields of the different protoenstatite phases (see Fig. 7) is analogous to that of respective phases in orthopyroxenes and clinopyroxenes. In the lowest density phase, usually at high temperatures, the silicate chains may be fully extended in the *c* direction or are slightly O-rotated (Thompson 1970). In the $MgSiO_3$ system, this structural feature is observed in *Pbcn* protoenstatite and *C*2/*c* high-*T* clinoenstatite. When pressure is increased, the rotation of the chains increases until suddenly every second chain changes its sense of rotation from O- to S-type. This phase change reduces the symmetry of the crystal from space group *Pbcn* to $P2_1cn$ in protopyroxene and similarly from *C*2/*c* to $P2_1/c$ (low-clinoenstatite) in clinopyroxene. At even higher pressures, it becomes energetically favorable to have only S-rotated chains. The respective high-pressure phases are *Pbcn*-II protoenstatite and *C*2/*c* high-*P* clinoenstatite.

In orthopyroxenes, the periodic unit along the *a* direction comprises two layers of silicate chains, which leads to more complex behavior. Interestingly, there seem to be two low-pressure phases with *Pbca* symmetry, the well-known orthoenstatite and a high-temperature phase that was observed recently (Ohi et al. 2008). In the $MgSiO_3$ system up to pressures of about 20 GPa, change of rotation sense is only expected in one of these layers (Jahn 2008). The first high-pressure transition leads to a structure where 25% of the chains S-rotated. The respective space group changes from *Pbca* to $P2_1ca$. At higher pressure, all chains in every second layer are S-rotated, which leads again to a structure with space group *Pbca* (Jahn 2008).

The transformation mechanism between protoenstatite and high-*P* clinoenstatite is similar to that of the orthoenstatite to high-*P* clinoenstatite transition studied before (Jahn and Martoňák 2008). As shown in Figure 8, shear deformations are activated in two different (100) planes. In the lower plane (Figs. 8a–8b), three intermediate stacking faults with high energies are identified (Fig. 6). Displacements are observed in both (100)[010] and (100)[001] directions. The total displacement vector after four shear deformations amounts to 1/3[001] + [010] in

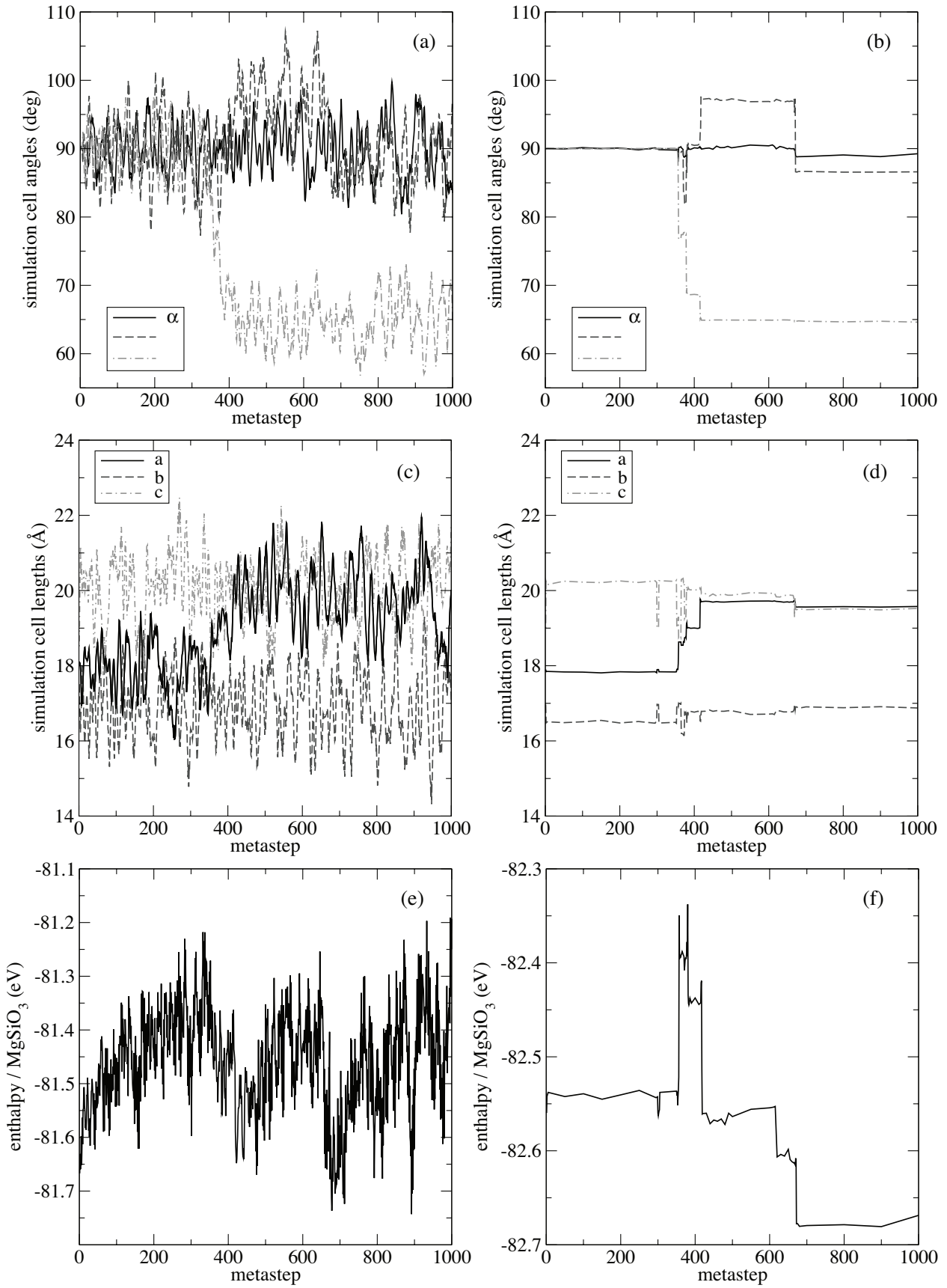

FIGURE 6. Evolution of simulation cell angles, cell lengths, and enthalpy during metadynamics at P = 15 GPa and T = 1000 K (**a**, **c**, and **e**), and after relaxing the cell to hydrostatic conditions at P = 15 GPa and T = 300 K (**b**, **d**, and **f**).

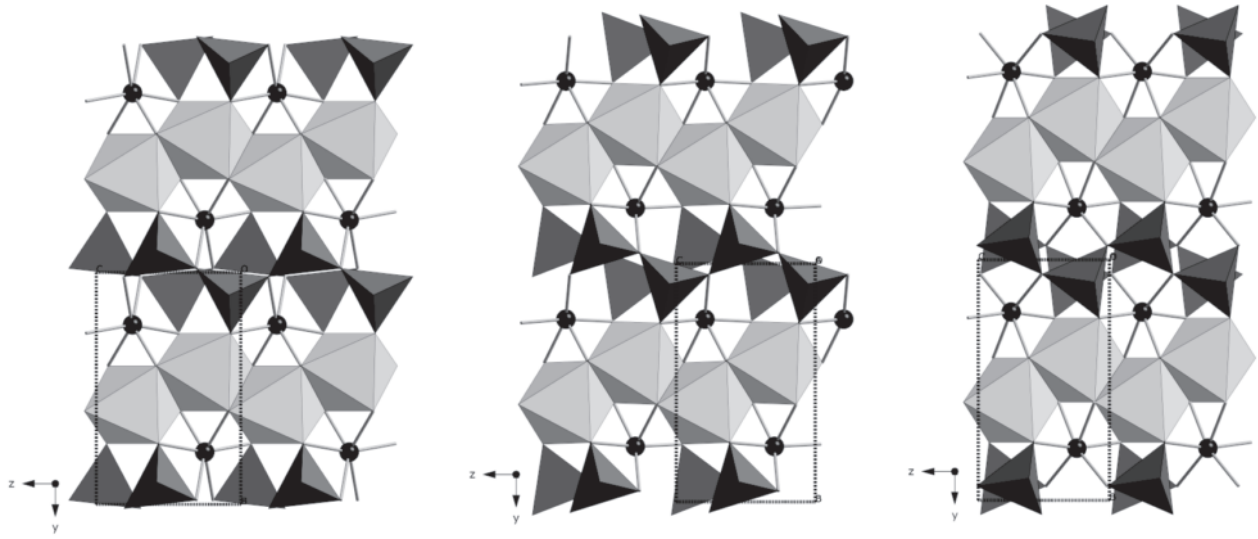

FIGURE 7. Polyhedral representation of the structural differences between protoenstatites of *Pbcn* (left), $P2_1cn$ (center), and *Pbcn*-II (right) type. Whereas in *Pbcn* there is only one type of O-rotated chains, alternating S- and O-rotated chains exist in $P2_1cn$. In the very high-pressure phase, *Pbcn*-II, there is again only one type of chains but with S-rotation. Dark gray = SiO_4 tetrahedra; light gray = MgO_6 octahedra (M1 site); balls = Mg on M2 site.

(100) and is equal to one of the shear deformations found in the transition from orthoenstatite to high-*P* clinoenstatite (Jahn and Martoňák 2008). Experimental evidence for the occurrence of a similar set of intermediate stacking faults during deformation of orthoenstatite is given in van Duysen et al. (1985). In the latter case, the stacking faults are associated with partial dislocations, which we cannot observe in the type of simulation used in this study.

The second shear in the upper (100) plane (Figs. 8b–8c) is of a different character since it only involves a single deformation in (100)[001] and the shear is in the opposite direction. This mechanism is consistent with macroscopic observations using transmission electron microscopy and has been used to discuss the ortho- to low- clinoenstatite transition (Coe and Kirby 1975; McLaren and Etheridge 1976). At this stage we cannot state which of the two mechanisms is more likely for the transition considered here. Both are consistent with the required changes in stacking order and especially with the reorientation of the M1 octahedra. We have some indications that the transition mechanism depends on pressure and temperature, but this issue will be the subject of further studies.

In conclusion, the combination of various atomic scale simulation techniques has provided unprecedented insight into the complex phase behavior of protopyroxenes. Isosymmetric polymorphs seem to be common for this structural family as well as for other pyroxene structures. Our results follow the

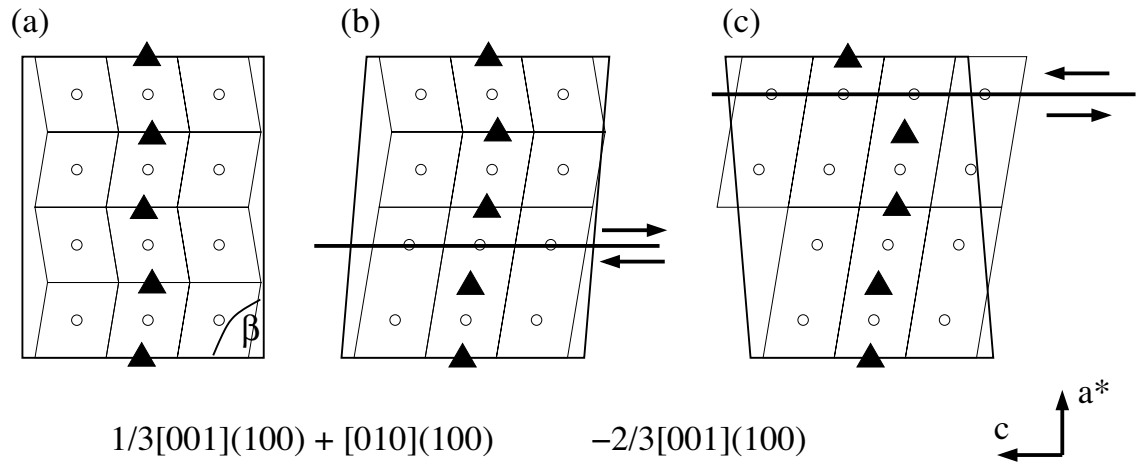

FIGURE 8. Schematic representations of the transformation mechanism from protoenstatite (**a**) to clinoenstatite (**c**) along (010). The intermediate structure (**b**) is found after the first set of shear deformations and corresponds to metastep 500 in Figure 6. The horizontal line and arrows indicate the (100) plane where the deformation happens and the direction of the slip, respectively. Magnesium layers are represented by circles and selected silicate chains by triangles. The angle β is a simulation cell parameter.

systematics of subsequent structural changes with pressure and/or temperature as described by Downs (2003). From the results of metadynamics simulations, two possible shear mechanisms are proposed for the phase transition from protoenstatite to high-*P* clinoenstatite. The results are consistent with experimental data and crystallographic considerations. However, for a more quantitative analysis, e.g., of the transition or defect energies, the relation between the shear of two extended half-crystals as modeled in the simulations and the slip due to the propagation of dislocations as expected in real systems still needs to be studied in more detail.

Acknowledgments

We thank Robert Downs and Patrick Cordier for very useful comments during the review process. Part of this work (S.J.) was supported by grant JA 1469/4-1 of the German Science Foundation (DFG). R.M. was partially supported by grants no. APVV-0442-07, VVCE-0058-07, VEGA 1/0096/08, and the Centre of Excellence of the Slovak Academy of Sciences (CENG).

References cited

Aguado, A., Bernasconi, L., Jahn, S., and Madden, P.A. (2003) Multipoles and interaction potentials in ionic materials from planewave-DFT calculations. Faraday Discussions, 124, 171–184.

Anderson, D.L. (1989) Theory of the Earth. Blackwell, Boston.

Angel, R.J., Chopelas, A., and Ross, N.L. (1992) Stability of high-density clinoenstatite at upper-mantle pressures. Nature, 358, 322–324.

Boysen, H., Frey, F., Schrader, H., and Eckold, G. (1991) On the proto- to ortho-/clino enstatite phase transformation: Single crystal X-ray and inelastic neutron investigation. Physics and Chemistry of Minerals, 17, 629–635.

Coe, R.S. and Kirby, S.H. (1975) The orthoenstatite to clinoenstatite transformation by shearing and reversion by annealing: Mechanism and potential applications. Contributions to Mineralogy and Petrology, 52, 29–55.

Coe, R.S. and Müller, W.F. (1973) Crystallographic orientation of clinoenstatite produced by deformation of orthoenstatite. Science, 180, 64–66.

Downs, R.T. (2003) Topology of the pyroxenes as a function of temperature, pressure, and composition as determined from the procrystal electron density. American Mineralogist, 88, 556–566.

Gonze, X., Beuken, J.-M., Caracas, R., Detraux, F., Fuchs, M., Rignanese, G.-M., Sindic, L., Verstraete, M., Zerah, G., Jollet, F., Torrent, M., Roy, A., Mikami, M., Ghosez, P., Raty, J.-L., and Allan, D.C. (2002) First-principles computation of material properties: The ABINIT software project. Computational Materials Science, 25, 478–492.

Gonze, X., Rignanese, G.-M., Verstraete, M., Beuken, J.-M., Pouillon, Y., Caracas, R., Jollet, F., Torrent, M., Zerah, G., Mikami, M., Ghosez, P., Veithen, M., Raty, J.-Y., Olevano, V., Bruneval, F., Reining, L., Godby, R., Onida, G., Hamann, D.R., and Allan, D.C. (2005) A brief introduction to the ABINIT software package. Zeitschrift für Kristallographie, 220, 558–562.

Henry, N.F.M. and Lonsdale, K., Eds. (1965) International Tables for X-ray Crystallography, Vol. I. Kynoch Press, Birmingham, U.K.

Hugh-Jones, D., Sharp, T., Angel, R., and Woodland, A. (1996) The transition of orthoferrosilite to high-pressure *C*2/*c* clinoferrosilite at ambient temperature. European Journal of Mineralogy, 8, 1337–1345.

Jahn, S. (2008) High-pressure phase transitions in $MgSiO_3$ orthoenstatite studied by atomistic computer simulation. American Mineralogist, 93, 528–532.

Jahn, S. and Madden, P.A. (2007) Modeling Earth materials from crustal to lower mantle conditions: A transferable set of interaction potentials for the CMAS system. Physics of the Earth and Planetary Interiors, 162, 129–139.

Jahn, S. and Martoňák, R. (2008) Plastic deformation of orthoenstatite and the ortho- to high-pressure clinoenstatite transition: A metadynamics simulation study. Physics and Chemistry of Minerals, 35, 17–23.

Kung, J., Li, B., Uchida, T., Wang, Y., Neuville, D., and Liebermann, R.C. (2004) In situ measurements of sound velocities and densities across the orthopyroxene → high-pressure clinopyroxene transition in $MgSiO_3$ at high pressure. Physics of the Earth and Planetary Interiors, 147, 27–44.

Lin, C.-C. (2003) Pressure-induced metastable phase transition in orthoenstatite ($MgSiO_3$) at room temperature: A Raman spectroscopic study. Journal of Solid State Chemistry, 174, 403–411.

Madden, P.A., Heaton, R., Aguado, A., and Jahn, S. (2006) From first-principles to material properties. Journal of Molecular Structure: THEOCHEM, 771, 9–18.

Martoňák, R., Donadio, D., Oganov, A., and Parrinello, M. (2006) Crystal structure transformations in SiO_2 from classical and ab initio metadynamics. Nature Materials, 5, 623–626.

Martyna, G.J., Tobias, D.J., and Klein, M.L. (1994) Constant pressure molecular dynamics algorithms. Journal of Chemical Physics, 101, 4177–4189.

McLaren, A.C. and Etheridge, M.A. (1976) A transmission electron microscopy study of naturally deformed orthopyroxene. I. Slip mechanisms. Contributions to Mineralogy and Petrology, 57, 163–177.

Monkhorst, H.J. and Pack, J.D. (1976) Special points for Brillouin-zone integrations. Physical Review B, 13, 5188–5192.

Ohi, S., Miyake, A., Shimobayashi, N., Yashima, M., and Kitamura, M. (2008) An isosymmetric phase transition of orthopyroxene found by high-temperature X-ray diffraction. American Mineralogist, 93, 1682–1685.

Perdew, J.P. and Zunger, A. (1981) Self-interaction correction to density-functional approximations for many-electron systems. Physical Review B, 23, 5048–5079.

Presnall, D.C. (1995) Phase diagrams of Earth-forming minerals. In T.J. Ahrens, Ed., Mineral Physics and Crystallography: A Handbook of Physical Constants, 2, p. 248–268. AGU Reference Shelf, American Geophysical Union, Washington, D.C.

Rappe, A.M., Rabe, K.M., Kaxiras, E., and Joannopoulos, J.D. (1990) Optimized pseudopotentials. Physical Review B, 41, 1227–1230.

Ringwood, A.E. (1975) Composition and Petrology of the Earth's Mantle. McGraw-Hill, New York.

Schrader, H., Boysen, H., Frey, F., and Convert, P. (1990) On the phase transformation proto- to clino-/orthoenstatite: Neutron powder diffraction. Physics and Chemistry of Minerals, 17, 409–415.

Thompson Jr., J.B. (1970) Geometrical possibilities for amphibole structures: model biopyriboles. (Recent discussions of pyroxenes and amphiboles.) American Mineralogist, 55, 292–293.

Thompson, R.M. and Downs, R.T. (2003) Model pyroxenes I: Ideal pyroxene topologies. American Mineralogist, 88, 653–666.

van Duysen, J.C., Doukhan, N., and Doukhan, J.C. (1985) Transmission electron microscope study of dislocations in orthopyroxene $(Mg,Fe)Si_2O_6$. Physics and Chemistry of Minerals, 12, 39–44.

Yang, H., Finger, L.W., Conrad, P.G., Prewitt, C.T., and Hazen, R.M. (1999) A new pyroxene structure at high pressure: Single-crystal X-ray and Raman study of the *Pbcn*-$P2_1cn$ phase transition in protopyroxene. American Mineralogist, 84, 245–256.

Manuscript received October 16, 2008
Manuscript accepted February 16, 2009
Manuscript handled by Artem Oganov